Change Detection Analysis Using Sentinel-1 Satellite Data with SNAP and GEE Regarding Oil Spill in Venezuela

Giacomo Caporusso(✉), Cristian Gallo, and Eufemia Tarantino

Department of Civil, Environmental, Land, Construction and Chemistry (DICATECh), Politecnico di Bari, Via Edoardo Orabona 4, 70126 Bari (BA), Italy
giacomo.caporusso@poliba.it

Abstract. In Venezuela, according to a report by the National Aeronautics and Space Administration (NASA) dated September 2021, up to 50,000 oil spills at sea have been monitored in the 2010–2016-time frame. In the current two-year period, the situation does not seem to have changed: the state refinery of the Venezuelan oil company Petróleos de Venezuela, S.A. (PDVSA), located near El Palito (Carabobo), is estimated to have been responsible for nearly 100,000 barrels of oil spilled in just one year. The aforementioned spills, with the intensification of extraction, transport and storage operations, have given rise to a greater number of accidents resulting in uncontrolled dispersion of material, endangering local marine-coastal ecosystems. The one that took place in July 2020 stands out, reconstructed a posteriori using satellite images that have highlighted its geo-environmental impact. Remote sensing has played a fundamental role in identifying and monitoring the spread of hydrocarbons; in the present study, the same event was analysed using Sentinel-1 Synthetic Aperture Radar Image (SAR) Change Detection techniques. The use of the desktop software SeNtinel Application Platform (SNAP) of the European Space Agency (ESA) made it possible to quantify the ocean surface affected by the phenomenon under analysis; at the same time, an algorithm was formulated within the cloud platform Google Earth Engine (GEE) which confirmed the same outputs but more quickly and allowed the implementation of an algorithm that exploits the statistical concept of value of Otsu threshold. The results obtained were subsequently compared with other results extrapolated through automatic methodologies developed by ESA, which supported a better accuracy of the procedures used in this study.

Keywords: Oil spill · Marine pollution · SAR · Sentinel-1 · SNAP · Google Earth Engine · El Palito · Otsu

1 Introduction

Accidental release of hydrocarbons, caused by offshore infrastructure and oil tankers, can have a significant and far-reaching environmental, social and commercial impact [1–3]. Therefore, promptly applying protocols aimed at containing the potential damage reported by marine and coastal environments, would be decisive: among the most

© The Author(s), under exclusive license to Springer Nature Switzerland AG 2022
O. Gervasi et al. (Eds.): ICCSA 2022 Workshops, LNCS 13379, pp. 387–404, 2022.
https://doi.org/10.1007/978-3-031-10545-6_27

common measures, the cleaning and recovery of the spill, the exact geolocation and the forecast of dispersion [4, 5]. To this end, in recent years, remote sensing technologies using radar-type satellite data have proved to be useful supports for the analysis of oil spills [6, 7]. Active remote sensing makes use of synthetic aperture radar sensors which are extremely advantageous, since the data can be acquired both day and night and in any atmospheric condition. Instead, passive remote sensing provides optical data for which an external light source (sun), cloudless and perturbation-free weather conditions are required [8, 9]. The presence of oil in the sea is manifested by a film of hydrocarbons on the water surface able to dampen the waves of the sea making it smoother [10]. Radar sensors record this condition with a lower backscatter energy intensity than natural marine conditions, causing dark streaks in the radar images depending on the quantities and types of spills and the dynamics of the ocean surface [11]. In some cases, distinguishing such spills from other contaminating factors could prove to be a particularly complicated operation, especially when dealing with rain cells, areas subject to weak wind or stains of biologic material [12, 13]. The investigated event refers to the accidental discharge of oil which took place around 26 July 2020 at the Venezuelan coast at the El Palito refinery. Sentinel-1 radar data from ESA's Copernicus program [14] was used within a Change Detection implemented both in the SNAP software and in the GEE cloud platform. The procedure consisted of a comparison between two different perfectly superimposable satellite images, one concomitant with the event and the other in the absence of hydrocarbon contamination and allowed the identification of the footprint area of the oil spill. In SNAP, the distinction between water and oil was evaluated through a backscatter threshold value deducible from the histogram statistics associated with the combination of images [15]. The speed of image processing in SNAP is strictly connected to the hardware characteristics of the device used: to get around this possible limit, it is convenient to opt for web-based and open-source cloud software, capable of managing a large amount of data and analysis directly online based on server processing in much shorter times, such as GEE [16]. Therefore, in GEE, given the need to distinguish only the two components of water and oil within the image, it was found appropriate to resort to the well-known Otsu algorithm [17], although little used for these study cases. It follows that the results obtained in both SNAP and GEE are more accurate and precise than those deriving from the automatic methodology implemented in the SNAP software, which is based exclusively on the processing of a single image concomitant to the event [18].

2 Material and Methods

2.1 The Study Area

The case study concerned the accident that occurred near the El Palito refinery, in the state of Carabobo, located near the Venezuelan coast [19] (Fig. 1). In this case, the ability to monitor, detect and manage oil spills is vital due to the persistent dangers posed to marine biodiversity, wildlife and habitats [20].

The start of the spill took place around 26 July 2020, but was silenced by the media, due to the lack of reporting by the PDVSA refinery and to the greater visibility of a simultaneous spill located off the coast of Mauritius which took place on 25 July [21].



Fig. 1. Area affected by the spill on Google Earth Pro.

The lack of preparation and the inability to act in the face of similar scenarios on the part of local realities was remarked by Eduardo Klein, associate professor at the department of environmental studies at the Simón Bolívar University (USB) in Caracas. His studies on the subject allowed him to reconstruct what was happening, also using satellite research conducted by the "Remote Sensing and Geo-Spatial Analysis Laboratory", a research hub of USB [20]. The results were both instructive and alarming: based on the TerraSAR-X satellite image (Fig. 2) of 26 July, the spill remained concentrated in the immediate vicinity of the refinery (coast of Carabobo), during which time there was no measures were taken to prevent its advancement towards Morrocoy National Park and other endangered coasts. The beginning of what Klein has renamed "ecocide" has taken the form of a "language of death", so nicknamed by the same, with an extension of about 260 km^2 and a maximum length of 27 km, in front of the refining centre [20, 22].

2.2 Dataset

Despite the existence of numerous increasingly performing commercial satellites, such as the previously mentioned TerraSAR-X one, the future of Remote Sensing seems to be oriented in the use of Open Data, among which are the products of the Sentinel-1 mission [23]. The latter was built in 2014 by ESA through the Copernicus project: it consists of the two satellites Sentinel-1A and Sentinel-1B. Both satellites describe a sun-synchronous orbit and are combined in such a way as to obtain a reduced temporal resolution from 12 to 6 days. In addition, they are equipped with C-band SAR technology, operating at a central frequency of 5.405 Ghz, with an image acquisition phase independent of weather and lighting conditions [8]. The modality with which the images are obtained is divided into single polarization (VV or HH) and double polarization (VV-VH and HH-HV) [24]. In favour of users, the most used data are above all those belonging to level I, i.e., the SLC and GRD products [23]. The difference between the latter is in the type of pre-processing present. The SLC products, in fact, less processed upstream, are the result of the Instrument Processing Facility (IPF) used for raw and compressed data.

This processing consists in the application of a series of algorithms that allow to obtain SAR data of amplitude and phase focused, georeferenced and provided in slant-range geometry [25]. GRD products, on the other hand, only contain the amplitude

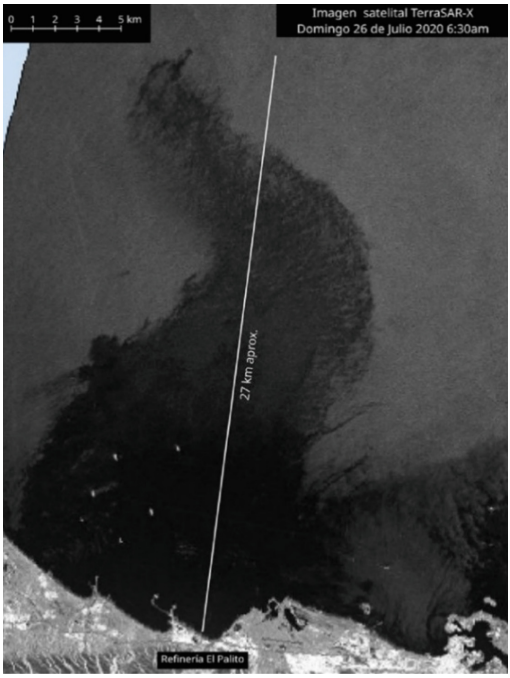


Fig. 2. TerraSAR-X radar image of 26 July 2020 processed by USB. https://newsbeezer.com

data and undergo refinement and cleaning procedures, such as a first filtering of the speckle and a Multilooking operation, which allows for square pixels [26]. The satellite images used for the case study were acquired free of charge through NASA's Alaska Satellite Facility Data Search (ASF) portal. The first data refers to a concomitant image of the event acquired on 31 July 2020. The scene shows a situation in which the spot, compared to July 26, has already moved away from the coast from which it originated and has spread to the open sea. The second image was acquired after the event, or on February 20, 2021. The choice is because it was preferred to work with both products belonging to S1A, in Descending mode, to be able to carry out interferometric operations as well. The images chosen for the study are both SLC and GRD type, with the aim of making a comparison between the surface results. Furthermore, this choice was also due to the need to ascertain the effects of the pre-processing carried out upstream on the GRD data on the final outputs [27].

2.3 SNAP Analysis

A first analysis of the event focused on the use of the Sentinel-1 toolbox of the SNAP open-source platform, software that supports the reading, visualization, processing and writing of data relating to various satellites [14]. This platform is widely used by researchers in the field of remote sensing with the intent of processing data through automatic procedures, such as the one served by ESA's toolbox for Oil Spill Detection, and semi-automatic procedures, such as the one used in the study proposed [26]. In

Fig. 3, the graph containing all the pre-processing and processing procedures for the SLC and GRD images, for the Master and Slave products, is presented.

2.4 Pre-processing

After the selection and acquisition of the satellite images, a series of semi-automatic preliminary processing was performed in order to make the data suitable for the actual processing phase. The pre-processing operations carried out on the two different inputs are reported [28].

Apply Orbit File: The orbital state vectors, contained in the metadata of SAR products, are generally not accurate. The correct orbits of the satellites are determined after several days are made available on SNAP only after the generation of the product. Through this operation it is possible to automatically download the OSV file from the ESA GNSS Hub which allows the orbital state vectors to be updated in the metadata, providing accurate information on the position and speed of the satellite [29].

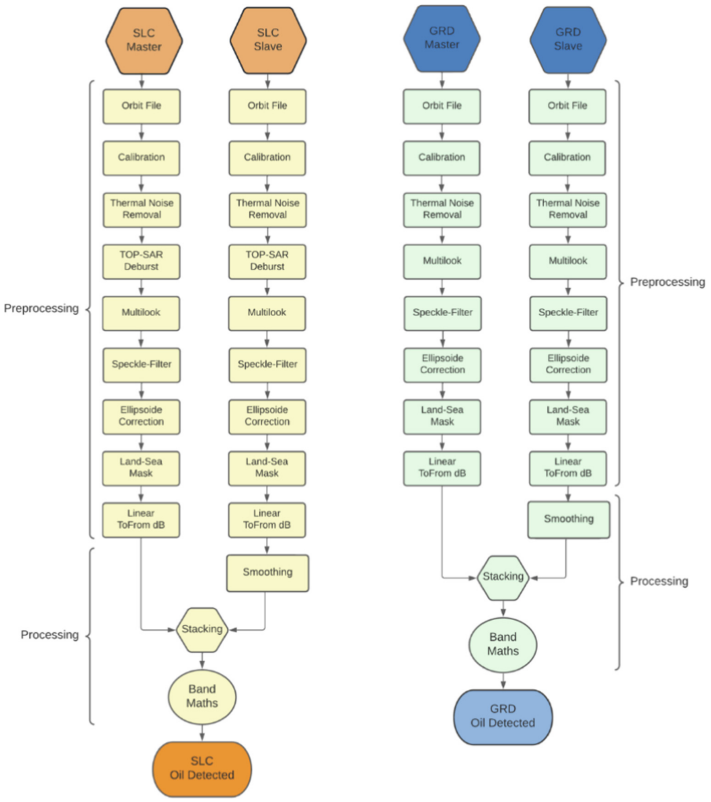


Fig. 3. SLC and GRD process workflow.

Calibration: Calibration is the procedure that converts the digital pixel values into radiometrically calibrated back-scatter values, since, in the typical first level radar data processing, a significant distortion remains. In particular, the process converts the radar reflectivity into physical units, referred to the plane perpendicular to the direction of the propagation beam. Therefore, it is necessary to apply radiometric correction to SAR products, so that the pixels numerically represent the radar backscatter value of the reflecting surface [29].

Thermal Noise Removal: Operation intended to remove the additional thermal noise of which a radar image is characterized. The removal of thermal noise reduces the distorting effects in the texture of the sub-swaths, normalizing the backscatter signal within the entire scene, favouring its reading in multi-swath acquisition mode [29].

TOP-SAR Deburst: The SAR detection devices carry out a progressive scan of the terrain through a series of images with which the data are acquired: this operation is called TOPSAR. Subsequently, the data acquired along the antenna beam are sampled in multiple adjacent sub-bands, shared by the same pixel spacing. The Debursting operation performs a merge of the adjacent bursts returning a single image by exploiting the azimuth overlap of the individual bursts. This operation is not performed for GRD images, since, being obtained from an SLC image, the operation will already be completed in the ESA pre-processes [30].

Multilook: A feature that unites digital images is the presence of the speckle; one of the objectives of these processes is to reduce any radiometric distortions present, which are shown through a "salt and pepper" effect. To achieve this, part of the initial resolution of the data must be renounced: in fact, through the multilooking operation, the original resolution is degraded, along the range direction and/or the azimuth direction, obtaining, on the other hand, pixels of a square [29]. For the case in question, the analysis was diversified for the two types of products. In addition to improving the interpretability of the image, a significant reduction in processing times is achieved [29].

Speckle-Filter: SAR images have an inherent granular noise that degrades image quality and makes interpretation of its characteristics more difficult. This trend is caused by the constructive and destructive interference of waves reflected by elementary scatters within each resolution cell. Speckle filtering is a procedure for increasing image quality by reducing such spots. In the case analysed, the use of the more innovative Lee Sigma filter was chosen, with Windows Size equal to 7×7 [31].

Ellipsoid Correction: In the SAR image there may be lateral distortions of distances and geometries, due to topographical variations and the angle of incidence of the satellite sensor. Ellipsoid Correction allows you to correct these discrepancies between the image and the real surface [32]. In particular, by operating in the sea, it is possible to approximate the real surface to an ellipsoid to make the necessary corrections within the image. The correction function is implemented through the Geolocation-Grid (GG) method which operates according to the procedures of a Range Doppler Terrain Correction [26].

Land-Sea Mask: Applies a mask that transforms all the pixels on the earth into "no data value", keeping only the pixels present on the liquid surface. The procedure consists of a quick comparison with the DEM downloaded from the software, which, by analysing the height of the pixel, will determine whether the position occupied is on the mainland or not. The operation is advantageous both in terms of processing times, significantly reduced due to the lightening of the image, and for the lack of consideration of possible false positives due to the presence of pixels that behave in a similar way to oil in terms of backscatter [32].

Linear To From dB: As the last step in the pre-processing workflow, the backscatter coefficient displayed in the Digital Number (DN) is converted to decibels (dB) through a logarithmic transformation. With this transformation, the product is made more readable by linearizing it [33]. At the end of the pre-processing workflow, clean and visibly more readable images were obtained, both for the pair of SLC products and for the GRDs, ready for subsequent processing (Fig. 4).

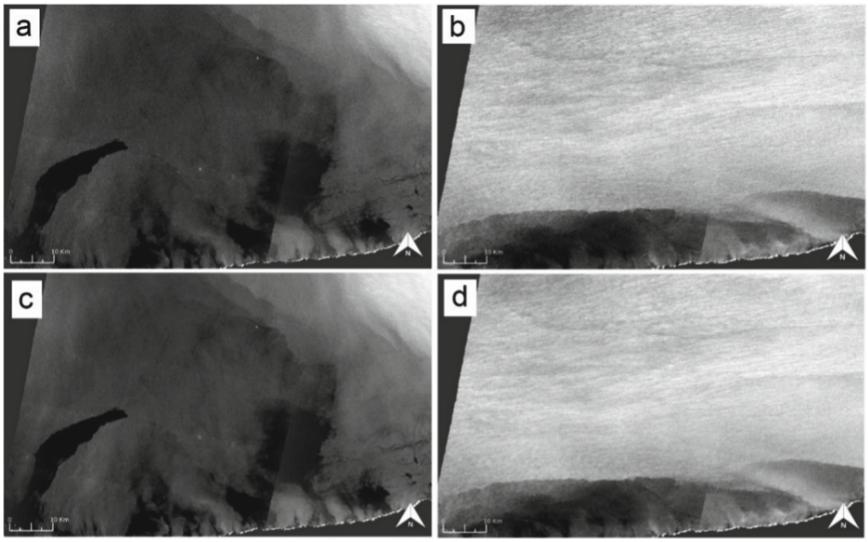


Fig. 4. Output after the SLC, Master (a) and Slave (b) image pre-processing phases, and GRD, Master (c) and Slave (d) images.

2.5 Processing

Following the SAR data pre-processing operations, products are obtained ready for processing activities through which it will be possible to recognize the spilled oil surface. Considering that oil particles have a greater influence on the amplitude of the radar signal, the analysis will be based on the latter [34].

Stacking: The toolbox interferometric modules provide for the registration of one (or more) "Slave" images with respect to a "Master" reference image [35]. This process requires, between the "Master" image and the various specificities of the "Slave" images, common characteristics called Tie Points, used as reference points for the entire operation. Following the use of a polynomial function that aligns the images, a single product ready for comparison is obtained in which the deformations of the reference image are spatially superimposed (in the geographic raster) to that of the base image. This occurs through a resampling method which, in this study, involved bilinear interpolation [36]. The co-registration procedure is completely automatic: in addition to the definition of the processing parameters, no further inputs or interventions by the user are required, as the optimization procedure is performed automatically for both images, perfecting the offsets of the operation [28]. In the proposed study, the Master data is represented by the data acquired on 07/31/2020, in which the incriminated event is present while the Slave data is represented by the image of 02/20/2021, in which there is total absence of oil.

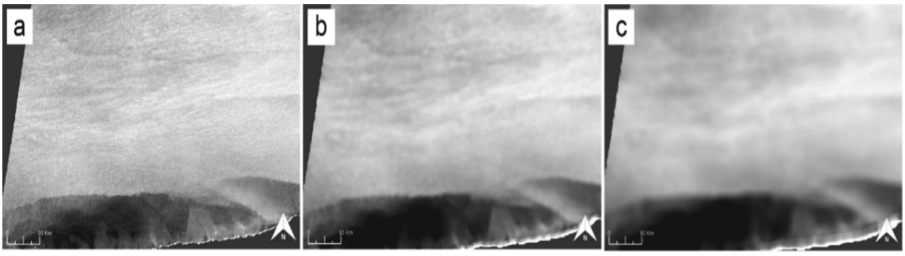


Fig. 5. Pre-processed GRD Slave image: without Smoothing filter (a), with Smoothing 10 × 10 (b) and with Smoothing 20 × 20 (c).

Smoothing: The speckle present in the SAR images compromises the precision of the deductible results [37]. The process, therefore, aims to "control" the intensity of the pixel backscatter values, helping to focus on the average of the values assumed in the same kernel [38]. The softening of the image tends to make the study area more homogeneous through a high-frequency detail filtering operation [39]. The median blurring filter assigns an average value to the pixels contained in the kernel, replacing it with the previously assumed values [40]. As the size of the matrix increases, the smoothing of the image will increase, thus obtaining different filtering effects. The operation was carried out exclusively for the Slave image, as we can say with certainty that it has pixels containing mainly water and therefore are approximately similar to each other. A series of various filtering windows was considered for the analysis, setting the kernel size of (5 × 5), (10 × 10), (15 × 15), (20 × 20) and (30 × 30) (Fig. 5). The choice of this filter was found to be the most effective for phenomena related to oil spill detection [41].

2.6 Change Detection Analysis and Threshold Values Definition

The comparison between the two pre-processed radar images is the basis of the Change Detection methodology [32]. The determination of the surface of floating hydrocarbons

for the image was referred to both the SLC and GRD images using different threshold values. These values were statistically determined through a polygonal geometry within which only the petroleum pixels fall (Fig. 6). This was certainly favoured by the shape of the spot, which can be enclosed in a single geometry defined as "region of interest" (ROI), not being characterized by an irregular or fragmented shape.

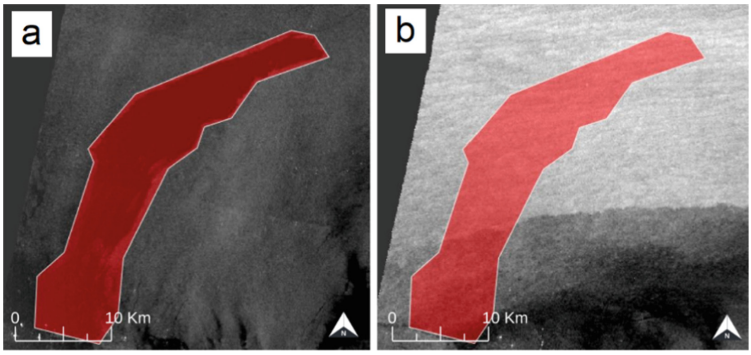


Fig. 6. ROI used to determine the threshold for the Master (a) and Slave (b) image.

Therefore, the determination of the threshold values referred to the SLC and GRD images refers to the backscatter values detected within the polygon. In particular, both the average value and the 90th percentile were considered due to the presence of some pixels characterized by anomalous backscatter values (outliers). The threshold values therefore arise from the difference between the values assumed in the ROI of the Master image and in the ROI of the Slave image.

The values for the SLC product and the GRD product are shown in Table 1.

Table 1. Threshold value.

Threshold SLC		
	Mean value (dB)	P90 value (dB)
ROI master	−27.568	24.783
ROI slave	−18.400	−16.372
Threshold	−9.168	−8.411
Threshold GRD		
	Mean value (dB)	P90 value (dB)
ROI master	−28.077	−24.978
ROI slave	−18.437	−16.341
Threshold	−9.639	−8.637

By doing so, four threshold values were obtained and subsequently used in the Change Detection. To extract the dark area that represents the release of hydrocarbons, a difference is initially made between the VV band of the Master image and the VV band of the Slave image using the Band Maths tool. The difference raster obtained is used to discriminate the "oil" pixels from the "water" pixels. This is done again through the Band Maths operator in which an inequality is set between the raster difference VV and the various thresholds. Subsequently, to calculate the area relating to the oil spill in each case, the "oil" pixels were counted using a mask.

2.7 Tool SNAP: Oil Spill Detection

The SNAP software provides the user with a collection of graphs containing preset algorithms that can be used for specific analyses. As part of the radar application, a toolbox is provided for the fully automatic mapping of oil spills, called "Oil Spill Detection". The algorithm has the substantial difference of not using Change Detection operations, going to operate exclusively on the image where the presence of the floating hydrocarbon surface is indicated. The composition of the workflow (Fig. 7) includes a first phase of image pre-processing in which only Land-Sea Mask and calibration operations are envisaged, in which a speckle filter is applied [41]. Subsequently, an image processing activity began, consisting of an operation called Oil Spill Detection, in which the "dark spots" are identified using the Adaptive Threshold Algorithm, an adaptive algorithm for calculating the Threshold based on single reference image only [42]. The survey ends with the final phase of Oil Spill Clustering, where the pixels are collected in clusters and selected with respect to the minimum size chosen by the user or performed with predefined parameters. The tool provides for the use of an average local backscatter value through the comparison Background Window Dimension freely left to the user: the software will define the pixels that will have a backscatter value lower than the one chosen [43].

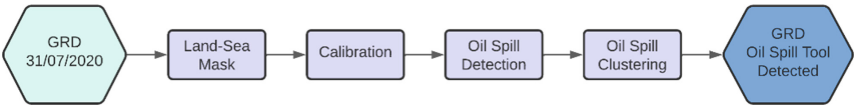


Fig. 7. SNAP oil spill detection tool workflow.

2.8 Change Detection in GEE e Threshold di OTSU

In the analysis previously carried out, the importance of lightening the processing burden was deduced in order to reduce the duration of processing times, depending on the type of hardware available to the user. The latter has often been considered a limitation of the attempt to expand the pool of users interested in the analysis of satellite images [44]. To ensure greater efficiency of these services and speed up the mechanical and repetitive phases of the process, the online platform Google Earth Engine (GEE) was created in 2011 [45]. In the study, an innovative algorithm was developed to improve

and facilitate the remote sensing of floating oil surfaces in the sea. The first operation involves uploading the Sentinel-1 image collections, importing the reference data present on the Earth Engine Data Catalog, in the Work Space. From the present collection, the availability of Sentinel-1 products exclusively of the GRD type is denoted: the SLC data, in fact, are not currently supported by the GEE platform [46]. In the GEE environment, from the Copernicus/S1_GRD collection, "analysis-ready" products are imported, already pre-processed, and containing measurements of the backscattering coefficient σ0 expressed in decibels (dB). The pre-processing steps (implemented by Sentinel-1 Toolbox) to derive the backscatter coefficient in each pixel are as follows [47]: Apply Orbit File, GRD Edge Noise Removal (has the task of removing low-intensity noise and invalid data on the edges of the scene), Thermal noise reduction, Radiometric calibration, Orthorectification and Multilook. Once the data collection has been imported, it is necessary to define the geometry of the area of interest on which to perform the calculations. A rectangle was therefore drawn, by imputing the coordinates of the four vertices, which consists of the Area of Interest (AOI) currently near El Palito and possibly translatable and modifiable in order to investigate other areas. Subsequently, the two products were selected through a series of Sentinel-1 Image Collection product filtering operations: type of VV copolarization, more effective than VH in detecting oil spills [48], IW acquisition method and Descending orbit. Once the filters have been applied, the two images referring to 07/31/2020 and 02/20/2021 are obtained, each of which has been associated with a layer of the GEE main window. The algorithm workflow also provides, before carrying out the Change Detection operations, an oil-free image smoothing operation. The "softening" of the image aims to make the study area more homogeneous through a filtering of the high-frequency pixel values [23]. The computation process, which in GEE is called convolution, performs a linear combination of the neighbouring pixels using a predefined set of weights. The results obtained are affected by the so-called "edge effect", produced by the fact that approaching the border of the image, the kernel applied to the pixel will not be totally occupied by other pixels that are part of the image [40]. To overcome this drawback, it was decided to apply this operation to a geometry with an offset of 0.02° from the margin of the previously selected one, in order to eliminate this effect. Subsequently, a comparison was made between the two radar images, the heart of the analysis based on the Change Detection methodology. The latter was processed by the Maths Operators present on GEE, which allow to obtain the Difference image, determined precisely by the subtraction, pixel by pixel, of the backscatter values of the two images purchased in the same AOI [49]. The threshold value considered was obtained using the Otsu algorithm, based on the analysis of variance between two classes of the single Difference image [50]. In satellite image analysis, there is often a need to use automated and data-driven methods to distinguish two relatively homogeneous objects, such as oil and water. For a single-band image with bimodal distribution of the pixels, it is possible to perform a two-class segmentation, finding a threshold that separates them. A bimodal image presents a plotting histogram of the backscatter values in two distinct distributions, almost separable from each other. In fact, between the two "fashions" it is possible to identify a local minimum point, in which the possibility of separating the histogram into two fronts could be considered. The binarization of Otsu, if properly performed, allows to obtain that value automatically [50]. The method,

therefore, is a means that automatically searches for an optimal threshold value, based on the distribution of the pixel values. Assuming therefore that the image histogram can be interpreted with two classes, the variance value between the classes is defined by the BSS (Between-Sum-of-Squares) value which is calculated using the formula [51]. The function examines every possible partition of the input data defined by the intensity of the histogram bins; therefore, it returns the mean associated with the bin that maximizes the BSS. The algorithm works best when you strategically choose a region in which the two classes are distributed approximately in equal proportions. After implementing the code, using the standard GEE library reducers, already included in the algorithm, the Difference image histogram was obtained: this also allowed us to estimate the average of the pixel distribution. By setting as discriminant, for the Change Detection operation, both the threshold determined with the Otsu algorithm and the average backscatter value assumed by the pixels of the difference image, it was possible to determine the number of pixels with a value equal to 1 all inside of a binary mask. This last step was carried out through a counting operation of the single class of pixels, thanks to which the floating oil surface was determined [46].

3 Results and Discussion

Based on the results obtained (Table 2), compared with the reference surface of about 260 km^2, detected on 26 July 2020 by the "Remote Sensing and Geo-Spatial Analysis Laboratory" of the USB, the proposed method found with successful oil surfaces.

Table 2. Surface analysis.

SNAP						GEE		
SLC			GRD			GRD		
Thres. (dB)	Sm. filter (pixel)	Δ (%)	Thres. (dB)	Sm. filter (pixel)	Δ (%)	Thres. (dB)	Sm. filter (pixel)	Δ (%)
P90 (−8.41)	NO	1.83	SNAP Oil Spill	NO	−38.04	OTSU (−9.50)	NO	43.06
	5	−1.13	P90 (−8.64)	NO	−0.85		15	6.78
	10	−3.78		10	−4.72		30	6.67
	15	−5.13		20	−7.40	Mean (−7.19)	NO	80.37
Mean (−9.17)	NO	−21.84	Mean (-9.64)	NO	−22.08		15	76.47

Within the table, the results obtained for the different platforms used are first distinguished, namely the SNAP desktop platform and the GEE cloud platform. Below, there is a further subdivision for the type of products used SLC and GRD. Also reported are the threshold values used in the study, any smoothing filter used, indicating the size of the kernel, and the surface deviation in percentage from the comparison surface.

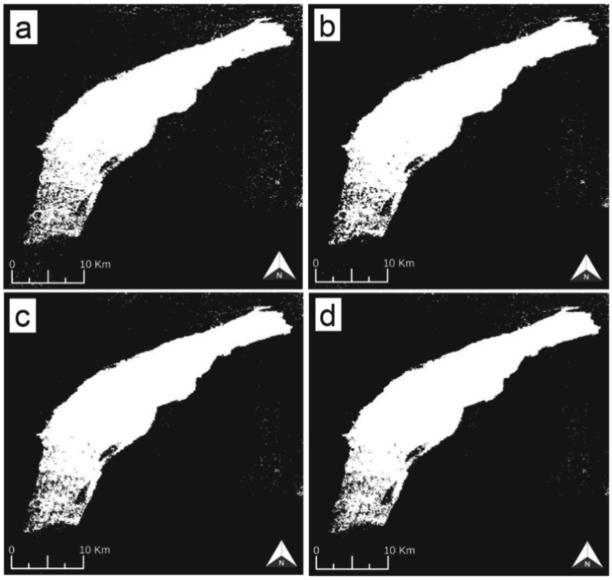


Fig. 8. Output of the Change Detection in SNAP of SLC images for threshold values P90: without Smoothing filter (a), with a Smoothing of 5 × 5 (b), with a Smoothing of 10x10 (c) and with a Smoothing of 15 × 15 (d).

Through SNAP (Fig. 8, 9, 10) compared to SLC products, using a 90th percentile threshold value from the statistical analysis of the histogram of the raster difference, with a smoothing filter with a kernel size equal to 5 × 5 on the oil-free image, a percentage difference of −1.13% with respect to the reference value. The result found with a threshold value defined by the simple average of the backscatter values within the polygon, instead, determines a percentage difference of −21.84%. For GRD products, however, a percentage deviation of −0.85% from the image with a threshold equal to the 90th percentile is reported without any smoothing filter applied. Also, for GRD products, the mean threshold value does not provide appreciably valid results considering the deviation of −22.08% from the reference value.

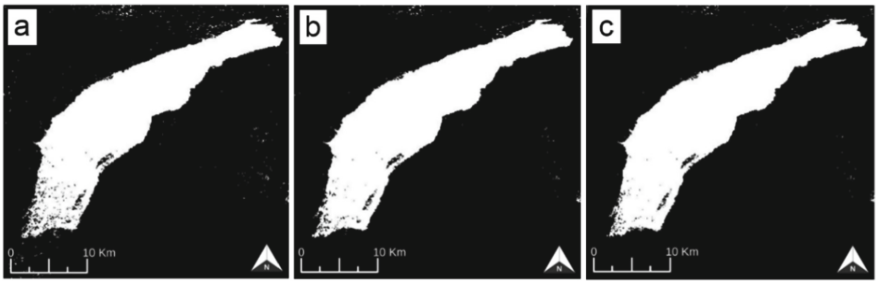


Fig. 9. SNAP Change Detection output of GRD images for P90 threshold values: without Smoothing filter (a), with a Smoothing of 10 × 10 (b) and with a Smoothing of 20 × 20 (c).

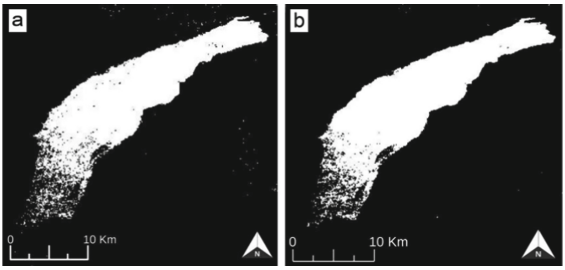


Fig. 10. Output of the Change Detection in SNAP for the threshold value referred to the average of the pixels without Smoothing filter of SLC (a) and GRD (b) images.

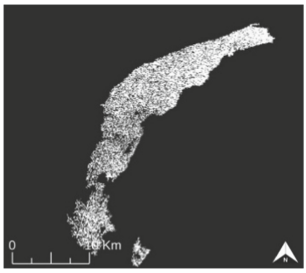


Fig. 11. Single image Oil Spill Tool output integrated into SNAP.

From the integrated single image "Oil Spill Tool" (Fig. 11) present in SNAP, a deviation equal to 38% from the comparison surface value is obtained. The cause also lies in the fact that some pixels escape the detection of the tool, as, due to the high computational capabilities required, the applied cluster is unable to "fill" the perimeter of the detected spot. It is also noted that some pixels with an oil-like behaviour are identified as oil (false positives); this is mainly due to shadowing effects, related to the presence of waves near the coast, and to the use of an adaptive algorithm for determining the threshold based on a single image [52].

Finally, the output layers from the GEE platform are reported (Fig. 12). From the analysis of the reported results, the significance of the result obtained using the algorithm devised by Otsu to determine the Threshold considered, which allows for an output that deviates by 6.67% from the reference value, is evident. To obtain a cleaner image, a Smoothing filter was applied to the event-free image which led to an important screening of false positives.

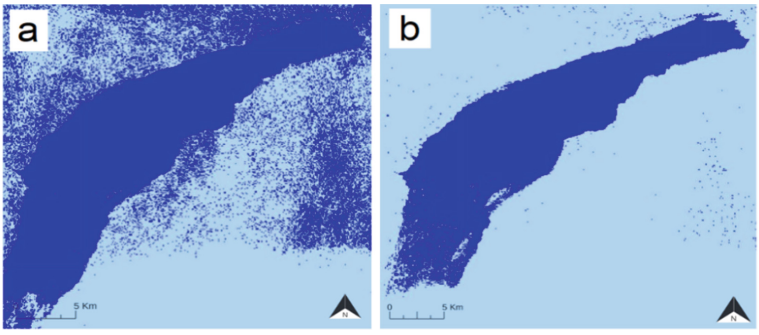


Fig. 12. GEE output with smoothing filter, Kernel size 15, with different Thresholds: OTSU value (left) and mean value (right).

Instead, the Change Detection which concerned the use of the threshold of the average pixel backscatter values, is not very effective with large areas of analysis. This result is due to a higher concentration of pixel values with a higher back-scatter value (water)

which led to a higher threshold value and a deviation of more than 76% from the reference surface.

4 Conclusions

The main objective of this study was to describe and compare alternative methodologies and procedures for monitoring oil spills using open-source tools (SNAP, Google Earth Engine) and open-source radar images (Sentinel-1 SAR). The results obtained clearly show how crucial it is to carry out correct assessments on the threshold value to be taken, since, despite the work platform and the type of product used, it is the real discriminating factor for a correct and efficient Oil Spill Detection. The determination of this value requires an analysis based on statistical methods and parameters that go beyond the single average of the backscatter values assumed by the image pixels, which does not always provide fairly accurate results. The Change Detection method is more appropriate for evaluating changes in the investigated surface, allowing us to state that an automated methodology referring to a single reference data, such as the one used by the SNAP Tool, cannot offer totally satisfactory results, as, the oil detection is often influenced by the presence of double and therefore not suitable to be performed with default software parameters. The study shows that, by moving to the GEE platform, the analysis in the EO sector turns out to be more versatile and faster, from a computational point of view, compared to desktop systems, characterized by often long and redundant operations. The new algorithm presented, conceived for the case in question, has allowed to obtain a considerable automation of the process, allowing large-scale data processing in a short time. To make the process even more direct and reliable was the use of the Otsu algorithm; through this method, classification results clearly better than the threshold dictated by the average value of the pixels were obtained. Given the ever-increasing use of GEE as part of remote sensing compared to other competing platforms, thanks to the previously mentioned advantages, we are trying to intervene to eliminate the deficiencies present in the system [49].

References

1. Yu, F., Sun, W., Li, J., Zhao, Y., Zhang, Y., Chen, G.: An improved Otsu method for oil spill detection from SAR images. Oceanologia **59**(3), 311–317 (2017)
2. Naboureh, A., Ebrahimy, H., Azadbakht, M., Bian, J., Amani, M.: RUESVMs: an ensemble method to handle the class imbalance problem in land cover mapping using Google Earth Engine. Remote Sens. **12**(21), 3484 (2020)
3. Venezuela's coastal villages, fisherman suffer as oil spills rise, Reuters. https://www.reuters.com/business/environment/venezuelas-coastal-villages-fisherman-suffer-oil-spills-rise, Accessed 06 Oct 2021
4. Sánchez, J.C.: Afectacion de los ecosistemas marino-costeros por los derrames de hidrocarburos marine-coastal ecosystems pollution by hydrocarbon spills. Comisión Editorial (2020)
5. Gorelick, N., Hancher, M., Dixon, M., Ilyushchenko, S., Thau, D., Moore, R.: Google earth engine: planetary-scale geospatial analysis for everyone. Remote Sens. Environ. **202**, 18–27 (2017)

6. Cervelli, E., Pindozzi, S., Capolupo, A., Okello, C., Rigillo, M., Boccia, L.: Ecosystem services and bioremediation of polluted areas. Ecol. Eng. **87**, 139–149 (2016)
7. Palladino, M., Nasta, P., Capolupo, A., Romano, N.: Monitoring and modelling the role of phytoremediation to mitigate non-point source cadmium pollution and groundwater contamination at field scale. Ital. J. Agron **13**(s1), 59–68 (2018)
8. Klein, E.: La refinería El Palito está todo el tiempo derramando hidrocarburos. https://elestimulo.com/eduardo-klein-la-refineria-el-palito-esta-todo-el-tiempo-derramando-hidrocarburos, 21 Aug 2020
9. Kingston, P.F.: Long-term environmental impact of oil spills. Spill Sci. Technol. Bull. **7**(1–2), 53–61 (2002)
10. Al-Ruzouq, R., et al.: Sensors, features, and machine learning for oil spill detection and monitoring: a review. Remote Sens. **12**(20), 3338 (2020)
11. Solberg, A.H., Brekke, C., Husoy, P.O.: Oil spill detection in Radarsat and Envisat SAR images. IEEE Trans. Geosci. Remote Sens. **45**(3), 746–755 (2007)
12. Capolupo, A., Pindozzi, S., Okello, C., Fiorentino, N., Boccia, L.: Photogrammetry for environmental monitoring: the use of drones and hydrological models for detection of soil contaminated by copper. Sci. Total Environ. **514**, 298–306 (2015)
13. Capolupo, A., Pindozzi, S., Okello, C., Boccia, L.: Indirect field technology for detecting areas object of illegal spills harmful to human health: application of drones, photogrammetry and hydrological models. Geospat. Health **8**(3), S699–S707 (2014)
14. Moreira, A., Prats-Iraola, P., Younis, M., Krieger, G., Hajnsek, I., Papathanassiou, K.: A tutorial on synthetic aperture radar. IEEE Geosci. Remote Sens. Mag. **1**(1), 6–43 (2013)
15. Capolupo, A., Nasta, P., Palladino, M., Cervelli, E., Boccia, L., Romano, N.: Assessing the ability of hybrid poplar for in-situ phytoextraction of cadmium by using UAV-photogrammetry and 3D flow simulator. Int. J. Remote Sens. **39**(15–16), 5175–5194 (2018)
16. Brekke, C., Solberg, A.H.S.: Oil spill detection by satellite remote sensing. Remote Sens. Environ. **95**(1), 1–13 (2005)
17. Kotova, L., Espedal, H.: Oil spill detection using spaceborne SAR- A brief review. Inf. Sustainabil., 791–794 (1998)
18. Tarantino, E.: Monitoring spatial and temporal distribution of Sea Surface Tempera-ture with TIR sensor data. Ital. J. Remote Sens./Rivista Italiana di Telerile-vamento **44**(1), 97–107 (2012)
19. ESA Mission Sentinel-1. https://www.esa.int, Accessed 01 Mar 2022
20. Akkartal, A., Sunar, F.: The usage of radar images in oil spill detection. Int. Arch. Photogramm. Remote Sens. Spat. Inf. Sci. **37**(B8), 271–276 (2008)
21. Espedal, H.: Detection of oil spill and natural film in the marine environment by spaceborne SAR. In: IEEE 1999 International Geoscience and Remote Sensing Symposium. IGARSS'99 (Cat. No. 99CH36293), vol. 3. IEEE (1999)
22. Villamizar, E.: Impactos de los derrames de petroleo sobre los arrecifes coralinos y sys bienes y sercivios ecosistémicos impacts of the oil spills over the coral reefs and their ecosistémicos impacts of the oil spills over the coral reefs and their ecosystems goods and services. Comision Editorial **45** (2020)
23. Mullissa, A., et al.: Sentinel-1 sar backscatter analysis ready data preparation in google earth engine. Remote Sens. **13**(10), 1954 (2021)
24. Migliaccio, M., Gambardella, A., Tranfaglia, M.: SAR polarimetry to observe oil spills. IEEE Trans. Geosci. Remote Sens. **45**(2), 506–511 (2007)
25. Torres, R., et al.: GMES Sentinel-1 mission. Remote Sens. Environ. **120**, 9–24 (2012)
26. Gancheva, I., Peneva, E.: Verification of the SNAP ocean-tool for oil spill detection for the Bulgarian Black Sea region. In: AIP Conference Proceedings, vol. 2075, no. 1. AIP Publishing LLC (2019)

27. Potin, P.: Sentinel-1 mission overview, pp. 04–11 (2011)
28. Giancaspro, A., Candela, L., Lopint, E., Lore, V.A., Milillo, G.: SAR images co-registration parallel implementation. In: IEEE International Geoscience and Remote Sensing Symposium, vol. 3. IEEE (2002)
29. Filipponi, F.: Sentinel-1 GRD preprocessing workflow. Multidisc. Dig. Publ. Inst. Proc. **18**(1) (2019)
30. Veci, L., Lu, J., Foumelis, M., Engdahl, M.: ESA's multi-mission sentinel-1 toolbox. In: EGU General Assembly Conference Abstracts (2017)
31. Fan, J., Zhang, F., Zhao, D., Wang, J.: Oil spill monitoring based on SAR remote sensing imagery. Aquatic Procedia **3**, 112–118 (2015)
32. Prastyani, R., Basith, A.: Utilisation of sentinel-1 SAR imagery for oil spill mapping: a case study of balikpapan Bay oil spill. J. Geospat. Inf. Sci. Eng. **1**(1), 22–26 (2018)
33. Nasirzadehdizaji, R., Cakir, Z., Sanli, F. B., Abdikan, S., Pepe, A., Calo, F.: Sentinel-1 interferometric coherence and backscattering analysis for crop monitoring. Comput. Electron. Agric. 185, 106118 (2021)
34. Nunziata, F., Gambardella, A., Migliaccio, M.: On the degree of polarization for SAR sea oil slick observation. ISPRS J. Photogramm. Remote. Sens. **78**, 41–49 (2013)
35. De Zan, F., López-Dekker, P.: SAR image stacking for the exploitation of long-term coherent targets. IEEE Geosci. Remote Sens. Lett. **8**(3), 502–506 (2010)
36. Li, Z., Bethel, J.: Image coregistration in SAR interferometry. Int. Arch. Photogramm. Remote. Sens. Spat. Inf. Sci. **37**, 433–438 (2008)
37. Ali, I., Cao, S., Naeimi, V., Paulik, C., Wagner, W.: Methods to remove the border noise from Sentinel-1 synthetic aperture radar data: implications and importance for time-series analysis. IEEE J. Sel. Topics Appl. Earth Obs. Remote Sens. **11**(3), 777–786 (2018)
38. Masoomi, A., Hamzehyan, R., Shirazi, N.C.: Speckle reduction approach for SAR image in satellite communication. Int. J. Mach. Learn. Comput. **2**(1), 62 (2012)
39. Zhu, J., Wen, J., Zhang, Y.: A new algorithm for SAR image despeckling using an enhanced Lee filter and median filter. In: 2013 6th International congress on image and signal processing (CISP), vol. 1. IEEE (2013)
40. Adrian, J., Sagan, V., Maimaitijiang, M.: Sentinel SAR-optical fusion for crop type mapping using deep learning and Google Earth Engine. ISPRS J. Photogramm. Remote. Sens. **175**, 215–235 (2021)
41. Longépé, N., Mouche, A.A., Ferro-Famil, L., Husson, R.: Co-cross-polarization coherence over the sea surface from sentinel-1 SAR data: perspectives for mission calibration and wind field retrieval. IEEE Trans. Geosci. Remote Sens. **60**, 1–16 (2021)
42. Liu, D., Yu, J.: Otsu method and K-means. In: 2009 Ninth International Conference on Hybrid Intelligent Systems, vol. 1. IEEE (2009)
43. Marghany, M.: RADARSAT automatic algorithms for detecting coastal oil spill pollution. Int. J. Appl. Earth Obs. Geoinf. **3**(2), 191–196 (2001)
44. Brigham, T.J.: Taking advantage of Google's Web-based applications and services. Med. Ref. Serv. Q. **33**(2), 202–210 (2014)
45. Tamiminia, H., Salehi, B., Mahdianpari, M., Quackenbush, L., Adeli, S., Brisco, B.: Google Earth Engine for geo-big data applications: a meta-analysis and systematic review. ISPRS J. Photogramm. Remote. Sens. **164**, 152–170 (2020)
46. Mutanga, O., Kumar, L.: Google earth engine applications. Remote Sens. **11**(5), 591 (2019)
47. Vollrath, A., Mullissa, A., Reiche, J.: Angular-based radiometric slope correction for Sentinel-1 on google earth engine. Remote Sens. **12**(11), 1867 (2020)
48. Chaturvedi, S.K., Banerjee, S., Lele, S.: An assessment of oil spill detection using Sentinel 1 SAR-C images. J. Ocean Eng. Sci. **5**(2), 116–135 (2020)

49. Xing, H., Hou, D., Wang, S., Yu, M., Meng, F.: O-LCMapping: a google earth engine-based web toolkit for supporting online land cover classification. Earth Sci. Inf. **14**(1), 529–541 (2021). https://doi.org/10.1007/s12145-020-00562-6
50. Yousefi, J.: Image Binarization Using otsu Thresholding Algorithm. University of Guelph, Ontario (2011)
51. Yang, X., Shen, X., Long, J., Chen, H.: An improved median-based Otsu image thresholding algorithm. Aasri Procedia **3**, 468–473 (2012)
52. Misra, A., Balaji, R.: Simple approaches to oil spill detection using sentinel application platform (SNAP)-ocean application tools and texture analysis: a comparative study. J. Indian Soc. Remote Sens. **45**(6), 1065–1075 (2017)